Contents lists available at ScienceDirect

Physica D

journal homepage: www.elsevier.com/locate/physd

Highlights

The Shannon entropy: An efficient indicator of dynamical stability

Physica D xxx (xxxx) xxx

Pablo M. Cincotta*, Claudia M. Giordano, Raphael Alves Silva, Cristián Beaugé

- The Shannon entropy provides a direct measure of the diffusion rate when dealing with chaos.
- A time-scale for physical instabilities can be derived.
- Its computation does not require the first variational equations.
- Applications to a 4D map and an example of the Three Body Problem are shown.
- Successful estimates of the time-scale of the instabilities are given.

Physica D xxx (xxxx) xxx

Contents lists available at ScienceDirect

Physica D

journal homepage: www.elsevier.com/locate/physd

The Shannon entropy: An efficient indicator of dynamical stability

Pablo M. Cincotta [a,*], Claudia M. Giordano [a], Raphael Alves Silva [b], Cristián Beaugé [c]

[a] Grupo de Caos en Sistemas Hamiltonianos, Facultad de Ciencias Astronómicas y Geofísicas, Universidad Nacional de La Plata and Instituto de Astrofísica de La Plata (CONICET), La Plata, Argentina
[b] Instituto de Astronomia, Geofísica e Ciências Atmosféricas, Universidade de São Paulo, Brazil
[c] Instituto de Astronomía Teórica y Experimental (IATE), Observatorio Astronómico, Universidad Nacional de Córdoba, Argentina

ARTICLE INFO

Article history:
Received 7 August 2020
Received in revised form 17 November 2020
Accepted 2 December 2020
Available online xxxx
Communicated by V.M. Perez-Garcia

Keywords:
Chaotic diffusion
Shannon entropy
4D maps
Three Body Problem

ABSTRACT

In this work it is shown that the Shannon entropy is an efficient dynamical indicator that provides a direct measure of the diffusion rate and thus a time-scale for the instabilities arising when dealing with chaos. Its computation just involves the solution of the Hamiltonian flow, the variational equations are not required. After a review of the theory behind this approach, two particular applications are presented; a 4D symplectic map and the exoplanetary system HD 181433, approximated by the Planar Three Body Problem. Successful results are obtained for instability time-scales when compared with direct long range integrations (N-body or just iterations). Comparative dynamical maps reveal that this novel technique provides much more dynamical information than a classical chaos indicator.

1. Introduction

Chaos indicators are powerful tools to investigate the global structure of phase space of dynamical systems. Most of them are based on the evolution of the tangent vector of a given trajectory as in case of the maximum Lyapunov Exponent (mLE).

Let $\varphi(t)$ be a given solution of a Hamiltonian flow. The mLE of φ is defined as

$$\mathrm{mLE}(\varphi) = \lim_{\substack{t\to\infty \\ \|\boldsymbol{\delta}(0)\|\to 0}} \frac{1}{t} \ln \frac{\|\boldsymbol{\delta}(\varphi(t))\|}{\|\boldsymbol{\delta}(0)\|}, \tag{1}$$

where $\boldsymbol{\delta}(\varphi(t))$ is the tangent vector to $\varphi(t)$ and it is the solution of the first variational equations of the Hamiltonian flow evaluated at $\varphi(t)$, with initial condition $\boldsymbol{\delta}(0)$. We refer to [1] for a theoretical discussion about the mLE and its computation.

It is well known, as it was discussed and shown in for instance [2,3] that in case of quasiperiodic motion, φ_q, after a motion time t, the finite time mLE, $\mathrm{mLE_t}$, converges to 0 as $\mathrm{mLE_t}(\varphi_q) \approx \ln t/t$, and for instance for $t = 10^4$, $\mathrm{mLE_t}(\varphi_q) \approx 10^{-3}$. On the other hand for a given chaotic motion, $\varphi_c(t)$, with $\mathrm{mLE} = \mu > 0$, $\|\boldsymbol{\delta}(\varphi_c(t))\| \approx \|\boldsymbol{\delta}(0)\| e^{\mu t}$. Thus by means of (1), to distinguish $\varphi_c(t)$ with $\mu \le 10^{-3}$ from $\varphi_q(t)$, the computational time should be $t \gtrsim 10^5$.

In the 90s, three techniques were widely used to investigate dynamics in phase space (particularly in Dynamical Astronomy): the mLE, the Frequency Map Analysis [4,5] and the Poincaré Surface of Section [6]. Computers were not fast enough to cope with the determination of the mLE for a large sample of orbits over long motion times. Thus fast dynamical indicators appear: the Fast Lyapunov Indicator, FLI [7–9]; the Mean Exponential Growth factor of Nearby Orbits, MEGNO [2,3,10]; the Smaller and the Generalized Alignment Indices, SALI–GALI [11–13]; the Orthogonal Fast Lyapunov Indicator, OFLI [14–16], among others.

Fast dynamical indicators are then useful to display the global dynamical structure of phase space unveiling the chaotic and regular components as well as the resonance web. Moreover they are able to show up invariant manifolds and provide a measure of hyperbolicity of the chaotic regions.

Though they provide information about the mLE in a given point of the phase space, it should be stressed that a positive mLE does not necessarily imply chaotic diffusion, i.e. a significant variation of the unperturbed actions or integrals of motion, the well known stable chaos is a typical phenomenon where the unstable motion is rather confined to small neighborhood of the initial values of the integrals over motion times larger than mLE^{-1} (see for instance [17] for an example in the Solar System). In many-body systems, some attempts to tackle this problem were proposed by means of a numerical technique based on the properties and the distribution of the deviation vector as discussed in [18,19].

Therefore chaos indicators are effective tools to conduct further relevant dynamical studies, for instance how effective is chaos to erase correlations among the phase space variables, i.e. to obtain an estimate of the time-rate of the instabilities

* Corresponding author.
E-mail addresses: pmc@fcaglp.unlp.edu.ar (P.M. Cincotta), giordano@fcaglp.unlp.edu.ar (C.M. Giordano), alves.raphael@usp.br (R. Alves Silva), cbeauge@unc.edu.ar (C. Beaugé).

https://doi.org/10.1016/j.physd.2020.132816

arising in the chaotic components of a divided phase space, the so-called chaotic diffusion.

Chaotic diffusion in high-dimensional Hamiltonian systems in both limits of weak and strong chaos has been largely investigated (see for instance the discussion given in [20] and references therein) while for studies in low dimensional systems we refer to [21–26].

In this work we take advantage of the Shannon entropy approach, already introduced in [27,28], to show that the entropy besides being an effective dynamical indicator, it provides an accurate measure of the diffusion rate. In the above mentioned works the theoretical framework is provided when dealing with the action space of high-dimensional systems. Moreover, successful applications of this novel technique to measure diffusion in two coupled rational standard maps [3], the Arnold Hamiltonian [29] and the planar restricted Three Body Problem were carried out.

On the other hand, in [25,26,30] it was shown analytically and numerically that the Shannon entropy is also a very powerful tool to measure correlations among the successive values of the phases involved in highly chaotic, almost ergodic, low dimensional maps as the whisker mapping and its generalization to cope with diffusion in Arnold model [21], and the standard map as well as the rational standard map, both for large values of the perturbation parameters.

Herein we focus our effort in the derivation of a time-scale for the chaotic instability in a 4D symplectic map that model the dynamics around the junction of two resonances of different order and in the HD 181433 exoplanetary system that could be well represented by the planar Three Body Problem.

2. The Shannon entropy formulation

In this section we summarize the formulation given in [25,27,28,31] regarding the Shannon entropy as a dynamical indicator as well as a measure of the diffusion rate in action space of high-dimensional Hamiltonian systems or symplectic maps. For a general background on the Shannon entropy we refer to [32,33] as well as [34].

Let us consider an N-dimensional system defined by actions $(I_1,\dots,I_N)$ and phases $(\vartheta_1,\dots,\vartheta_N)$. For simplicity and due to formal aspects of this presentation we assume a 4D map with $(I_1,I_2)\in\mathbb{R}^2, (\vartheta_1,\vartheta_2)\in\mathbb{T}^2$ and a given section $\mathcal{S}=\{(I_1,I_2): |\vartheta_1-\vartheta_1^0|+|\vartheta_2-\vartheta_2^0|<\delta\ll 1\}$ where $\vartheta_1^0,\vartheta_2^0$ are some fixed values of the phases that define $\mathcal{S}$.

A given trajectory $\gamma=\{(I_1(t),I_2(t)), t=1,\dots,\infty\}\subset\mathcal{S}$ leads to a surface distribution density on $\mathcal{S}$, $\rho(I_1,I_2)$ assumed normalized, such that introducing a partition of $\mathcal{S}$, $\alpha=\{a_k, k=1,\dots,q\}$, $q\gg 1$, the (disjoint) elements have a measure

$$\mu(a_k)=\int_{a_k}\rho(I_1,I_2)dI_1dI_2. \tag{2}$$

For finite but large motion times, $t\le N_s$, where N_s denotes the number of intersections of γ with $\mathcal{S}$ that will be the scenario hereafter, the above measure reads

$$\mu(a_k)=\frac{n_k}{N_s}.$$

where n_k is the number of action values (I_1,I_2) in the cell a_k. Thus the entropy of γ for the partition α is defined as

$$S(\gamma,\alpha)=-\sum_{k=1}^{q_0}\mu(a_k)\ln(\mu(a_k))=\ln N_s-\frac{1}{N_s}\sum_{k=1}^{q_0}n_k\ln n_k. \tag{3}$$

where $1\ll q_0\le q$ denotes the non-empty elements of the partition. It is simple to show that $0\le S\le\ln q_0$, the minimum occurs when $n_k=N_s, n_j=0\ \forall j\ne k$, i.e. a trajectory lying on a torus that reduce to a single point in $\mathcal{S}$, while the maximum corresponds to ergodic motion, $n_k=N_s/q_0\ \forall k$, all elements of the partition having the same measure. Thus, as it was shown in for instance [27], the entropy is in fact an effective indicator of the stability of the motion, comparisons with other fast dynamical indicators were given.

Let us focus first on nearly random motion. As it was discussed in [25,30], if n_k follows a Poissonian distribution with mean $\lambda=N_s/q_0\gg 1$, setting $n_k=\lambda+\xi_k$ with $|\xi_k|\ll\lambda$, then up to $\mathcal{O}((\xi_k/\lambda)^2)$, the entropy (3) for uncorrelated motion, say γ^r, reduces to

$$S(\gamma^r,\alpha)\approx\ln q_0-\frac{1}{2\lambda^2}\frac{1}{q_0}\sum_{k=1}^{q_0}\xi_k^2. \tag{4}$$

Recalling that the Poissonian fluctuations obey a normal distribution with mean value 0 and standard deviation $\sqrt{\lambda}$, then

$$\frac{1}{q_0}\sum_{k=1}^{q_0}\xi_k^2=\lambda, \tag{5}$$

and the entropy (4) reduces to

$$S(\gamma^r,\alpha)\approx\ln q_0-\frac{1}{2\lambda}. \tag{6}$$

Therefore for random motion $|S-\ln q_0|=\mathcal{O}(\lambda^{-1})$ being $\lambda\gg 1$, defining $S_0=\ln q_0$, the entropy can be well approximated by

$$S(\gamma^r,\alpha)\approx S_0.$$

In case of a strong unstable, chaotic but non-random trajectory, γ, we write $n_k=\lambda+\tilde{\xi}_k$ where we assume that $|\xi_k|<|\tilde{\xi}_k|\ll\lambda$. Then accordingly to (4)

$$S(\gamma,\alpha)\approx\ln q_0-\frac{1}{2\lambda^2}\frac{1}{q_0}\sum_{k=1}^{q_0}\tilde{\xi}_k^2, \tag{7}$$

recalling (5) and defining β such that

$$\sum_{k=1}^{q_0}\tilde{\xi}_k^2=\beta\sum_{k=1}^{q_0}\xi_k^2,$$

it follows then

$$\beta=\frac{\langle\tilde{\xi}_k^2\rangle}{\lambda},\qquad\langle\tilde{\xi}_k^2\rangle=\frac{1}{q_0}\sum_{k=1}^{q_0}\tilde{\xi}_k^2. \tag{8}$$

Thus, from (7)

$$|S(\gamma,\alpha)-\ln q_0|\approx\frac{\beta}{2\lambda}. \tag{9}$$

Thus defined, $\beta\ge 1$ is the ratio between the variance of the fluctuations of n_k and the mean value λ for a non-Poissonian distribution. Thus, also for γ, $S(\gamma,\alpha)\approx S_0$ provided that $\beta/\lambda\ll 1$.

On the other hand, in case of a trajectory γ^c confined to a small domain of $\mathcal{S}$, as it was discussed in [30,31], the distribution of the n_k approaches a delta, $\delta(n_k-\lambda)$, and thus estimating $|\xi_k|\approx 1/2$ (see [30]), it follows from (4) that

$$|S(\gamma^c,\alpha)-\ln q_0|\approx\frac{1}{8\lambda^2} \tag{10}$$

and thus it is also true that $S\approx S_0$ even though $\lambda\sim 1$.

Following [31], a local diffusion coefficient for γ in the interval $(t,t+\delta t)$ can be estimated from the time derivative of S whenever $dS/dt\approx dS_0/dt$,

$$D_S(\gamma,t):=\frac{\Sigma}{q}q_0(t)\frac{dS}{dt}(t)\approx\frac{\Sigma}{q}\frac{\delta q_0}{\delta t}(t), \tag{11}$$

Σ being the area of $\mathcal{S}$ where the partition is defined, so that Σ/q provides the size of the cells in action dimensions (see below for an alternative definition of Σ). The estimate (11) rests on the assumption that locally the variation of S is due to changes in the number of occupied cells, i.e. due to variations in the actions in the interval $(t, t+\delta t)$, in such a way that (see [27,31])

$$\delta q_0(t) \propto \langle \delta I_1^2(t) + \delta I_2^2(t) \rangle \approx D_t \delta t,$$

where $\langle \cdot \rangle$ denotes space average and $D_t \equiv D(I_1(t), I_2(t))$ is a local diffusion coefficient in action space, when γ is restricted to the region $(I_1, I_1+\delta I_1)\times(I_2, I_2+\delta I_2)$. In other words, any other source of changes in the entropy, for instance due to variations in the measure $\mu(a_k)$, is neglected.

Thus, a global diffusion coefficient for γ can be defined as

$$D_S(\gamma) := \lim_{t\to\infty} \frac{1}{t}\int_{t_0}^{t} D_S(\gamma, t)dt \approx \langle D_S(\gamma, t)\rangle_{t\le N_s}, \qquad (12)$$

where the last approximation applies in case of finite but large enough motion times.

This formulation has a free parameter, the number of elements of the partition q. In any case, the condition $q_0 \ll q$ is required so that $q_0(t)$ could increase with time. However its value mainly depends on the nature of the motion. If σ denotes the area covered by the diffusion in $\mathcal{S}$, we consider two different limiting situations, when (i) $\sigma \ll \Sigma$ and (ii) $\sigma \approx \Sigma$. In case (i), the area of the unit cell Σ/q, should be small with respect to σ in such a way the non-empty elements of the partition would have nearly the same invariant measure, so $q \gg \Sigma/\sigma \gg 1$. In other words, very small cells are required in order to have enough resolution such that the q_0 cells properly cover σ. When (ii) applies, $q \gg 1$ still holds. In [31] it was shown that the optimal choice of q in order to (11) and (12) work is that $N_s \lesssim q < N_s^{1/\hat{S}_L}$, where $\hat{S}_L$ is some threshold value of $\hat{S} = S/\ln q$, such that $\hat{S}_L < 1$.

Let us discuss in more detail the above condition. At first sight, the statistical approach would require that $N_s/q \gg 1$. However, as discussed above, the average λ involves q_0 not q, such that $q_0(t) \ll q\,\forall t$, so the condition $N_s/q \gg 1$ can be relaxed allowing $N_s/q \lesssim 1$ but $N_s/q_0 \gg 1$.

For the upper limit, being σ the area covered by the diffusion, then the mean (discrete) density is $\rho_0 = N_s/\sigma$. Therefore the mean distance between the iterates is $d \approx \sqrt{\sigma/N_s}$. On the other hand the linear size of the unit cell is $\Delta = \sqrt{\Sigma/q}$. If the diffusion is confined to a small region of $\mathcal{S}$, $\sigma \ll \Sigma$, we can assume that the n_k follows a nearly δ distribution, the density $\rho(I_1, I_2) \approx \rho_0\,\forall(I_1, I_2) \in \sigma$, is large and therefore q can be taken in such a way that $d < \Delta$. This condition leads to $q < (\Sigma/\sigma)N_s$, with $\Sigma/\sigma \gg 1$.

In this case of a nearly uniform distribution, the factor Σ/σ can be estimated as $q/q_0 \approx q^{1-\hat{S}}$, with $\hat{S} \le \hat{S}_L < 1$ and therefore the above condition reduces to $q < N_s^{1/\hat{S}_L}$. Thus, this upper bound for q implies that no empty cells appear in σ due to discrete character of ρ. Therefore whenever $\rho(I_1, I_2) \approx \rho_0$ and $\Sigma/q \ll 1$, D_S is almost invariant under a partition change while S increases with q (see [31] for numerical examples).

On the other hand, if the extension of the diffusion region in $\mathcal{S}$ is large, $\sigma \approx \Sigma$, a nearly Poissonian distribution applies. The density now is smaller (for the same number of iterates), the fluctuations are large ($\sim \sqrt{N_s/q_0}$) and thus in general $d > \Delta$ except if q is small enough, but small values of q are not allowed in this formulation since we require that q_0 grows with time. The estimate $\Sigma/\sigma \approx q/q_0$ is no longer true and thus no additional restriction appear to q. In this scenario D_S is not invariant under a change of the partition.

In the next sections we present applications of this approach to two different dynamical systems. We refer to [27,28,31] for particular examples concerning the time evolution of S, D_S for several initial conditions and different sets of parameters such as q, N_s on high-dimensional systems. In particular, an extensive investigation concerning the dependence of this approach on the parameters involved in its computation is addressed in [31].

3. Applications

In this section we present applications of the Shannon entropy approach to measure the diffusion rate in quite different models: a system of discrete time consistent in a 4D map and a system of continuous time, the Three Body Problem for a particular planetary system.

3.1. I. A system of discrete time

Following [35], we consider the 4-D symplectic map $\mathcal{M}$: $(I_1, I_2, \vartheta_1, \vartheta_2) \to (I_1', I_2', \vartheta_1', \vartheta_2')$, $I_j \in \mathbb{R}$, $\vartheta_j \in \mathbb{S}^1$ defined as

$$\begin{aligned} I_1' &= I_1 + \eta \sin\vartheta_1,\\ I_2' &= I_2 + \eta\varepsilon \sin\vartheta_2,\\ \vartheta_1' &= \vartheta_1 + \eta(I_1' + a_2 I_2'),\\ \vartheta_2' &= \vartheta_2 + \eta(a_2 I_1' + a_3 I_2'); \end{aligned} \qquad (13)$$

where $|\varepsilon| \ll 1, \eta \lesssim 2$ are real parameters and $a_2, a_3 \in \mathbb{Q}$. Actually, this map can be thought as a 4D generalization of the well known 2D standard map.

The application $\mathcal{M}$ can be regarded as the time-η map associated to the flow of the Hamiltonian

$$H(I_1, I_2, \vartheta_1, \vartheta_2) = \frac{I_1^2}{2} + a_3\frac{I_2^2}{2} + a_2 I_1 I_2 + \cos\vartheta_1 + \varepsilon\cos\vartheta_2. \qquad (14)$$

Actually, the map $\mathcal{M}$ not only provides the successive values of $(I_j(t_l), \vartheta_j(t_l))$ at $t_l = l\eta$, $l = 0, 1, \ldots, N$ generated by the Hamiltonian (14) but also the evolution of the actions and angles due to H plus a periodic time-dependent perturbation. Indeed, the discrete system derives from the differential equations

$$\begin{aligned} \dot{I}_1 &= \cos\vartheta_1 \times 2\pi\delta_{2\pi}(\tau),\\ \dot{I}_2 &= \varepsilon\cos\vartheta_2 \times 2\pi\delta_{2\pi}(\tau),\\ \dot{\vartheta}_1 &= I_1 + a_2 I_2,\\ \dot{\vartheta}_2 &= a_2 I_1 + a_3 I_2, \end{aligned}$$

where $\tau = 2\pi\eta^{-1}t$ and $\delta_{2\pi}$ is the 2π-periodic delta function defined through its Fourier expansion. The above set of equations corresponds to the flow of the Hamiltonian (see [26] for details concerning the numerical equivalence between the map and the Hamiltonian flow)

$$\mathcal{H}(I_1, I_2, \vartheta_1, \vartheta_2, \tau) = \frac{I_1^2}{2} + a_3\frac{I_2^2}{2} + a_2 I_1 I_2 + \sum_{k,k'=-\infty}^{\infty}[\cos(\vartheta_1 - k\tau) + \varepsilon\cos(\vartheta_2 - k'\tau)]. \qquad (15)$$

Thus $\mathcal{H}$ reduces to H when keeping only the terms in the sum with $k, k' = 0$. The frequencies of the system being

$$\omega_1(I_1, I_2) = I_1 + a_2 I_2, \qquad \omega_2(I_1, I_2) = a_3 I_2 + a_2 I_1, \qquad 2\pi\eta^{-1}. \qquad (16)$$

The parameter η, besides being the time step of the flow, defines the frequency of the external perturbation and thus it plays an important role in the dynamics of the system as we discuss below.

Both, the Hamiltonian (14) and the map (13) were introduced in [35] to investigate the dynamics near the intersection of two resonances of different order. In fact, H is a truncated normal form around the intersection of the resonances $I_1 + a_2 I_2 = 0$ and $a_2 I_1 + a_3 I_2 = 0$.

As it was shown in [35], the map $\mathcal{M}$ has four fixed points located at $p_1 = (0,0,0,0)$, $p_2 = (0,0,\pi,0)$, $p_3 = (0,0,0,\pi)$, $p_4 = (0,0,\pi,\pi)$; in particular if $c = a_3 - a_2^2$ then for $\varepsilon c > 0$ and $\eta \lesssim 2$, p_1 is unstable while p_4 is stable.

From (15) and (16), the full set of first order resonances is

$$\mathcal{R} = \{(I_1, I_2) : I_1 + a_2 I_2 = 2\pi k/\eta,\ a_3 I_2 + a_2 I_1 = 2\pi k'/\eta,\ k, k' \in \mathbb{Z}\}, \tag{17}$$

where the double resonance model H given by (14) corresponds to the resonances with $k = k' = 0$.

The map is invariant under the transformation $I_1 \to I_1 + I_1^m$, $I_2 \to I_2 + I_2^m$, with $I_1^m = 2\pi p/(\eta a_2)$, $I_2^m = 2\pi p'/(\eta a_3)$, where p, p' are integer numbers such that $p/a_2 \in \mathbb{Z}$, $p' a_2 = r a_3$ with r an integer number. Thus we can restrict the action space to $\mathcal{D} = (-I_1^m, I_1^m) \times (-I_2^m, I_2^m)$ with opposite sides identified and therefore $\Sigma = 4 I_1^m I_2^m$. In what follows we take $a_2 = 1/2, a_3 = 5/4$, so $p = 1, p' = 5$ $(r = 2)$, and thus the model corresponds to the crossings of resonances of order 3 and 7.

The separation between resonances depends on η, a_2 and a_3, being the latter

$$d_k = \frac{2\pi}{\eta\sqrt{1 + a_2^2}}, \qquad d_{k'} = \frac{2\pi}{\eta\sqrt{a_3^2 + a_2^2}},$$

for the lower and higher order resonances respectively. Large values of η would lead to a highly chaotic map due to the strong resonance interaction.

After the canonical transformations, $(I_1, I_2, \vartheta_1, \vartheta_2) \to (J_1, J_2, \varphi_1, \varphi_2)$ defined by

$$\varphi_1 = \vartheta_1, \quad \varphi_2 = \vartheta_2 - a_2\vartheta_1, \quad J_1 = I_1 + a_2 I_2, \quad J_2 = I_2$$

or $(I_1, I_2, \vartheta_1, \vartheta_2) \to (P_1, P_2, \psi_1, \psi_2)$ such that

$$\psi_1 = \vartheta_1 - a_2\vartheta_2/a_3, \quad \psi_2 = \vartheta_2, \quad P_1 = I_1, \quad P_2 = I_2 + a_2 I_1/a_3$$

the Hamiltonian (15) can be written in terms of the resonant Hamiltonian corresponding to the resonances $I_1 + a_2 I_2 = 0$ or $a_2 I_1 + a_3 I_2 = 0$,[1] as

$$\bar{\mathcal{H}}(J_1, J_2, \varphi_1, \varphi_2, \tau) = \frac{J_1^2}{2} + \frac{bJ_2^2}{2} + \cos\varphi_1 + \varepsilon\cos(\varphi_2 + a_2\varphi_1),$$

or

$$\tilde{\mathcal{H}}(P_1, P_2, \psi_1, \psi_2) = \frac{a_3 P_2^2}{2} + \frac{bP_1^2}{2a_3} + \varepsilon\cos\psi_2 + \cos(\psi_1 + a_2\psi_2/a_3),$$

revealing that the resonance half-widths are 2 and $2\sqrt{\varepsilon/a_3}$ respectively. A massive overlap of the low order primary resonances takes place when their separation is of the order of two times their half width, that is when $\eta > \eta_c = 0.5\pi(1 + a_2^2)^{-1/2}$, that for the a_2 value here considered $(a_2 = 0.25)$, leads to $\eta_c \approx 1.52$. On the other hand, the overlap of the high order resonances takes place when $(\eta^2\varepsilon)_c = 0.25\pi^2 a_3 (a_2^2 + a_3^2)^{-1}$. For instance, setting $\eta = 1 (\eta < \eta_c)$, $\varepsilon_c \approx 1.7$ Therefore under the condition $\eta < \eta_c$, $\varepsilon < \varepsilon_c$ and away from resonance crossings, the motion around the center of the resonances should be stable. Moreover, since we consider values of a_2, a_3 and ε such that $b\varepsilon > 0$, around the resonance intersection the dynamics is also stable since the fixed point p_4 is stable.

Considering the reduced map $\mathcal{M}$, i.e., $(I_1, I_2) \in \mathcal{D}$ with opposite sides identified and adopting comparatively small values of the parameters just to show the action space structure, say $\eta = 0.6$, $\varepsilon = 0.3$, the resonance web is shown in Fig. 1, where a fast dynamical indicator (the MEGNO, see [2,3,10]) was used for separate stable, regular motion from the chaotic regime (see [31] for different sets of parameters).

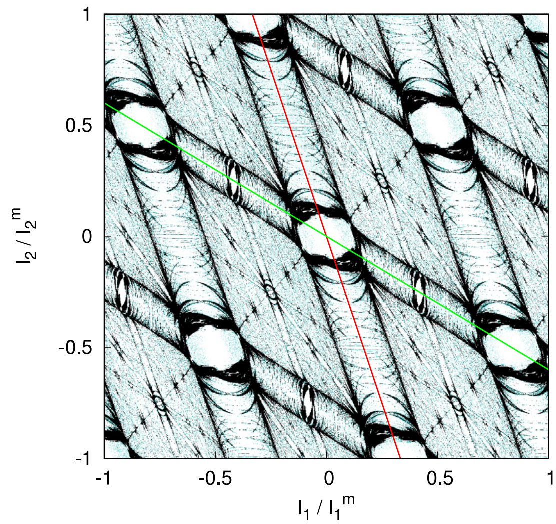

Fig. 1. Contour plot of the MEGNO for the map (13) for $a_2 = 0.5$, $a_3 = 1.25$ for $\varepsilon = 0.3$ and $\eta = 0.6$ after $N = 600$ iterates. The initial values of the phases are fixed to $\vartheta_1 = \vartheta_2 = \pi$ such that the stable fixed point at $(I_1, I_2) = (0,0)$ belongs to the section. The red line corresponds to the resonance $I_1 + a_2 I_2 = 0$ while the green one to $a_2 I_1 + a_3 I_2 = 0$. (For interpretation of the references to color in this figure legend, the reader is referred to the web version of this article.)

The center of the lower order resonance is drawn in red ($I_1 + a_2 I_2 = 0$) while the one for the higher order resonance appears in green ($a_2 I_1 + a_3 I_2 = 0$). The figure is a contour plot of the final values of the MEGNO after $N = 600$ iterates for an equispaced grid of 2000×2000 pixels for $(I_1, I_2) \in D$, with $\vartheta_1(0) = \vartheta_2(0) = \pi$ such that the stable fixed point at $(I_1, I_2) = (0,0)$ lies on this section, since $\varepsilon c > 0$ for the considered values of a_2 and a_3.

The final values of the MEGNO, $\langle Y \rangle$, are displayed such that light colors represent regular, periodic or quasiperiodic trajectories, $\langle Y \rangle \le 2$, while dark colors indicate unstable chaotic motion $\langle Y \rangle \approx \mu N/2 \gg 2$, where μ is the mLE of the corresponding trajectory. The actual resonance web is quite similar to the expected theoretical one. Besides the intersection at the origin between the low order resonance and the higher order one, several other resonances are present, those with $k, k' \neq 0$ that show up parallel to the latter. Note that all the crossings between these primary resonances are identical, their dynamical properties around each junction being the same as the one at the origin. Many other resonances, which are linear combinations of the three involved frequencies,

$$m_1\omega_1(I_1, I_2) + m_2\omega_2(I_1, I_2) + 2\pi m_3\eta^{-1} = 0, \qquad m_i \in \mathbb{Z}$$

can also be identified as very narrow channels.

A relevant aspect of this map is that diffusion along resonances occurs and thus it turns out interesting to investigate the time rates of the instabilities in $\mathcal{M}$, particularly along the primary resonances.

3.2. Diffusion

In this section we focus on the diffusion that takes place in the map (13) along the homoclinic tangle of the primary resonances, after adopting a section that includes the unstable fixed point p_4 and values of the parameter such that $\eta < \eta_c$, $\varepsilon < \varepsilon_c$.

Thus in what follows we adopt a section defined as $\mathcal{S} = \{(I_1, I_2) \in \mathcal{D} : \vartheta_1 = \vartheta_2 = 0\}$ and in order to avoid quite restricted

[1] All the resonances with $k, k' \neq 0$ are identical to those with $k, k' = 0$.

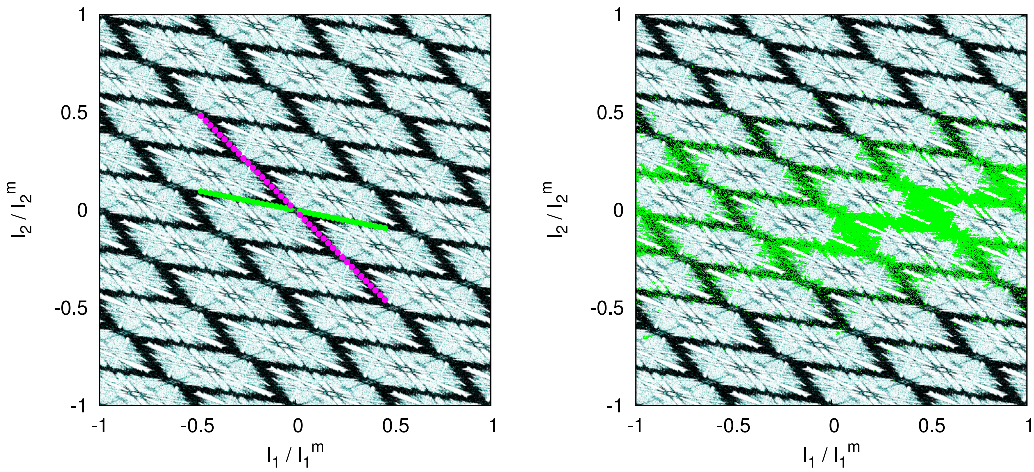

Fig. 2. Action space of the map $\mathcal{M}$ for $\varepsilon = 0.6, \eta = 0.7$ for initial values of the phases $\vartheta_1 = \vartheta_2 = 0$ and the selection of initial conditions, in magenta on the resonance $I_1 + a_2 I_2 = 0$ and in green on $a_2 I_1 + a_3 I_2 = 0$ (left). Observed diffusion for an initial ensemble located on the resonance $a_2 I_1 + a_3 I_2 = 0$ and for a section defined by $\mathcal{S} = \{I_1(k), I_2(k) : |\vartheta_1| + |\vartheta_2| < 0.02\}$ (right). (For interpretation of the references to color in this figure legend, the reader is referred to the web version of this article.)

diffusion we consider somewhat larger values of the parameters, $\varepsilon = 0.6$, $\eta = 0.7$, and take 40 initial conditions along the two main resonances. Fig. 2 (left) presents a MEGNO contour plot of $\mathcal{M}$ on $\mathcal{S}$ for the adopted values of the parameters as well as the selection of the initial conditions.

The considered values of η, ε are somewhat larger than the ones in Fig. 1 and the numerical experiments show that the diffusion spreads beyond the region $\Sigma = 4I_1^m I_2^m$ but mostly confined to the homoclinic tangles of the main resonances as Fig. 2 (right) shows for an ensemble of size 10^{-7} located on the resonance $a_2 I_1 + a_3 I_2 = 0$ centered at the largest value of $I_1(0)$. The iterates are depicted in green since the diffusion corresponds to an initial condition also plotted in green in Fig. 2 (left). In this example $|I_1| > I_1^m$, so the normalization constant Σ/q should be modified in such a way that it takes into account that σ could exceed Σ.

The spread of the diffusion for small ensembles located on both main resonances as well as the time evolution of S, D_S for this model and different values of the parameters are discussed in [31].

Let us proceed with a series of numerical experiments. First we iterate each of the initial conditions, $(I_1(0), I_2(0))$, on both resonances up to $N \leq 10^9$ and compute the time (or number of iterates) after which $|I_1| \geq I_1^m$ or $|I_2| \geq I_2^m$ on the section $\mathcal{S} = \{I_1(k), I_2(k) : |\vartheta_1| + |\vartheta_2| < 0.02\}$. In other words, we determine the actual escape time, $t_{\rm esc}$, as the time when the trajectory leaves $\mathcal{D} = (-I_1^m, I_1^m) \times (-I_2^m, I_2^m)$.

Later, we compute the average escape time $\langle t_{\rm esc} \rangle$ over small ensembles, typically $\sim 10^{-7}$, of $n_p = 100$ initial conditions centered around $(I_1(0), I_2(0))$ for $N \leq 5 \times 10^8$. The use of an ensemble to determine an average time would reduce stickiness effects and should provide a smooth dependence of $\langle t_{\rm esc} \rangle$ on the initial conditions.

Afterwards we compute D_S by means of (11) considering an ensemble of $n_p = 1000$ initial conditions around each of the 80 values of $(I_1(0), I_2(0))$ and after $N = 5 \times 10^6$, with $q = 2000 \times 2000$ using $I_j(t) \bmod(I_j^m)$ but also keeping the values of $I_j(t) \in \mathbb{R}$ in order to modify the normalization constant. For the numerical computation of the entropy and its time derivative, we take a sample interval $\delta t = 5 \times 10^3 \ll N$ and thus $(dS/dt)_{\rm num} = (S(t + \delta t) - S(t))/\delta t$. As mentioned since $|I_j|$ could exceed I_j^m, we replace $\Sigma = 4I_1^m I_2^m \to \Sigma_e \approx \sigma$, that we estimate by means of the maximum and minimum values attained by the actions, $\sigma \approx (I_1^{\rm max} - I_1^{\rm min})(I_2^{\rm max} - I_2^{\rm min})$. Indeed, whenever $\sigma > \Sigma$, the normalization constant in (12) should be modified in such a way that σ/q (instead of Σ/q) provides the effective area of the unit cell.

Thus, an escape time can be estimated as

$$t_{\rm esc}^S = K \frac{(I_1^m - I_1(0))^2 + (I_2^m - I_2(0))^2}{D_S}, \tag{18}$$

where the factor $K \sim 1$ takes into account the fact that $t_{\rm esc}^S$ depends on the escape route in action space on the section $\mathcal{S}$. Indeed, if for instance the escape occurs only along the resonance $a_2 I_1 + a_3 I_2$ in such a way that only $|I_1| > I_1^m$, the numerator in (18) should be modified as $I_2^m \to -a_2 I_1^m / a_3 < I_2^m$ and therefore the above definition of $t_{\rm esc}^S$ with $K = 1$ would overestimate the actual escape time. It is clear that this factor mainly depends on the dynamics of the system for the given values of the parameters that define the spread of the diffusion on the action space.

Finally, we also compute the ensemble variance over the $n_p = 1000$ initial conditions after $N = 5 \times 10^6$ iterates and numerically determine both, the exponent b and the coefficient D by recourse to a mean square fit on a power law $\mathrm{Var}(I_f) = Dt^b$, where I_f is a fast action, in this case $I_f^2 = I_1^2 + I_2^2$. The fit was done in $\ln(\mathrm{Var}(I_f)) = \ln(D) + b \ln t$, in a similar fashion as in [26] and [20] where both coefficients were derived in different systems. Whenever $b \approx 1$, D would lead to the expected diffusion coefficient provided that correlations among the phases are negligible. Thus an escape time can also be derived from the estimate of D, $t_{\rm esc}^V = K((I_1^m - I_1(0))^2 + (I_2^m - I_2(0))^2)/D$, for initial conditions on both resonances.

The linear fit was performed for each of the 80 ensembles of initial conditions and thus we expect a non-smooth behavior of D or $t_{\rm esc}^V$ and this would be mostly determined by the fit of b, the smaller b leads to the larger D. In any case we found $0.71 < b < 0.88$, as Fig. 3 reveals, so the diffusion is not normal, at least for the considered motion times. Therefore the diffusion coefficient D obtained by a numerical fit on the variance evolution would not provide a good measure of the actual diffusion rate provided by $t_{\rm esc}$ or $\langle t_{\rm esc} \rangle$. Maybe for much longer motion times the diffusion approaches a nearly normal regime as it was discussed in for instance [36].

Fig. 4 shows the results for $t_{\rm esc}$, $\langle t_{\rm esc} \rangle$, $t_{\rm esc}^S$, $t_{\rm esc}^V$. We set $K = 1/4$ in such a way that in (18), $(I_j^m - I_j(0))/2$ is the average distance traveled by the trajectories before the particles escape from $\mathcal{D}$. We observe that $t_{\rm esc}^S$ provides a good and smooth estimate of the actual escape time in comparison with t_{esc}. The values of $t_{\rm esc}^S$

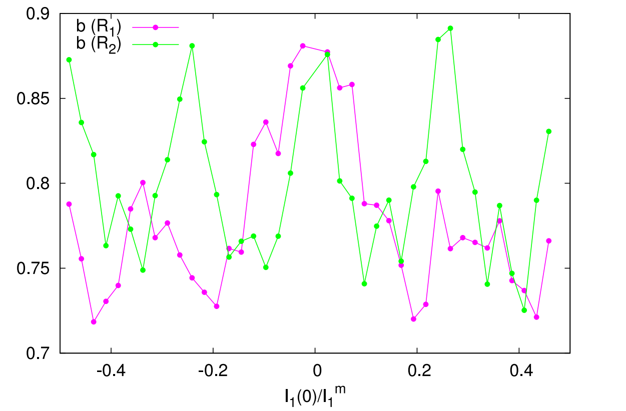

Fig. 3. Exponents obtained after a linear fit of $\mathrm{Var}(I_f) = Dt^b$ with $I_f^2 = I_1^2 + I_2^2$ for the selected initial conditions, in magenta on the resonance $R_1 : I_1 + a_2 I_2 = 0$ and in green on $R_2 : a_2 I_1 + a_3 I_2 = 0$. (For interpretation of the references to color in this figure legend, the reader is referred to the web version of this article.)

for initial conditions on both resonances are nearly the same, consistent with the periodicity of the map and the fact that the diffusion spreads over the same resonances.

The dispersion in the values of t_{esc} is due to stickiness; they strongly depend on the selected initial condition while $\langle t_{\mathrm{esc}} \rangle$ is smooth and nearly constant, it does not present significant oscillations and in any case t^S_{esc} is quite close to $\langle t_{\mathrm{esc}} \rangle$. The fluctuations in t^V_{esc} are similar to that observed in the exponent b and consequently opposite to D. Notice should be taken that the values t^V_{esc} underestimate the expected values $\langle t_{\mathrm{esc}} \rangle$, in some cases in about two orders of magnitude. When adopting different values of the parameters and initial conditions located away from the primary resonances, the estimates of t^S_{esc} completely agree with those obtained from $\langle t_{\mathrm{esc}} \rangle$ also for $K = 1/4$ as shown in [31].

3.3. II. A system of continuous time: The planar 3BP

Herein we present a stability analysis of the exoplanetary system HD 181433 [37–39], in the context of the planar three-body problem (3BP). We follow some considerations already presented in [31], but now focus on the relationship between a computed diffusion coefficient D_S and a global instability time-scale associated to specific initial conditions (ICs) in the phase space of the system.

A preliminary architecture for HD 181433 was firstly proposed in [37], a three-planetary system with minimum masses of $0.02M_{\mathrm{Jup}}$, $0.64M_{\mathrm{Jup}}$ and $0.54M_{\mathrm{Jup}}$, where M_{Jup} denotes Jupiter's mass. These planets are orbiting a K-type star with a mass of $0.86M_\odot$ [37], close to the Solar mass $M_\odot$. However, the obtained values for the eccentricities locate the two outer planets in trajectories of rather unstable character. Later on, new nominal solutions for the system were derived in [39] revealing an almost 7/1 mean motion resonance (MMR) between the two massive planets. According to [38] instead, such planets are placed near a 5/2 MMR.

Table 1
Three-planet solution for HD 181433 given in [39].

Parameter	Unit	HD 181433 b	HD 181433 c	HD 181433 d
m	$[M_{\mathrm{Jup}}]$	0.0223 ± 0.0003	0.674 ± 0.003	0.612 ± 0.004
a	[AU]	0.0801 ± 0.0001	1.819 ± 0.001	6.60 ± 0.22
e		0.336 ± 0.014	0.235 ± 0.003	0.469 ± 0.013
P	[day]	9.37452 ± 0.0002	1014.5 ± 0.6	7012 ± 276
ω	[deg]	210.4 ± 2.5	8.6 ± 0.7	241.4 ± 2.4
T_0	[day]	52939.16 ± 0.06	52184.3 ± 1.9	46915 ± 239

In the present work, we adopt the solution given in [39] that takes into account further data from recent observations. The concomitant orbital parameters are displayed in Table 1, which includes the masses (m), the semi-major axes (a), the eccentricities (e), the orbital periods (P), the arguments of pericenter (ω) and the time of passages at periastron (T_0). The mean anomalies M_i ($i = 1, 2, 3$) being obtained from the indicated values of T_0.

The proposed dynamical architecture of this system, with a small inner planet very close to the host star and two giant planets in wider orbits, may be approximated to a simpler model where the inner body is neglected; in fact, it is possible to verify, through numerical integrations, that the presence of the lighter body does not globally disturb the motion of the two external ones in long-term time-scales. Indeed, notice that the mass of planet b barely amounts $\sim$ 3% of the remaining masses and, as a consequence, its presence has almost no perturbation effect on the heavier bodies, which is specially true on taking into account the distance ratio between the inner planet and the external ones. This is a standard procedure in many exoplanetary systems with a similar structure, see for instance [40] for GJ 876. Anyway for illustrative purposes, Fig. 5 presents the evolution of the orbital parameters of the massive bodies when considering the 3 or 4 body problem, where the numerical integrations were carried out with a Bulirsh–Stoer integrator with a precision $ll = 12$. It becomes clear that the presence of the less massive body does not alter the global dynamics of planets c and d. Therefrom, the HD 181433 system can be studied in the framework of the 3BP, the host star with two orbiting bodies namely HD 181433 c and d (hereafter, we will use the subscripts 1 and 2 to indicate each one, respectively).

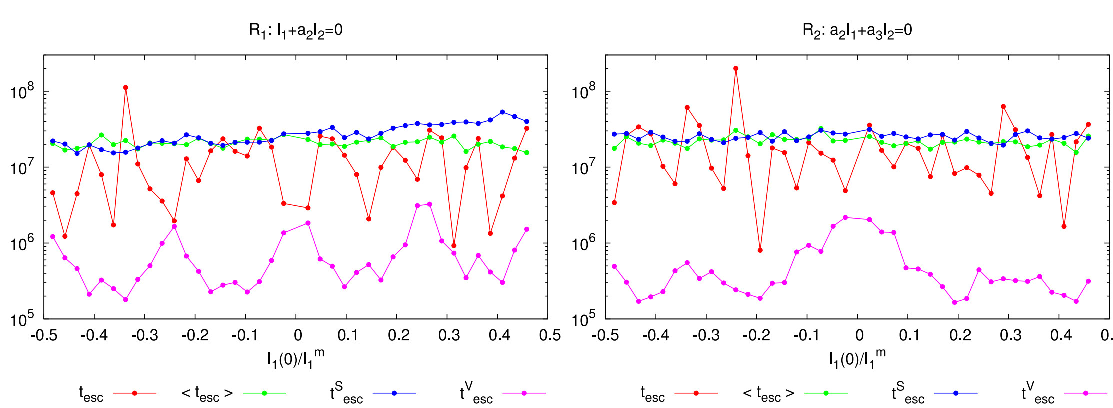

Fig. 4. Escape times in the map $\mathcal{M}$ for $\varepsilon = 0.6$, $\eta = 0.7$ and 40 initial conditions on the homoclinic tangle of the resonances $I_1 + a_2 I_2 = 0$ and $a_2 I_1 + a_3 I_2 = 0$ after setting $K = 1/4$.

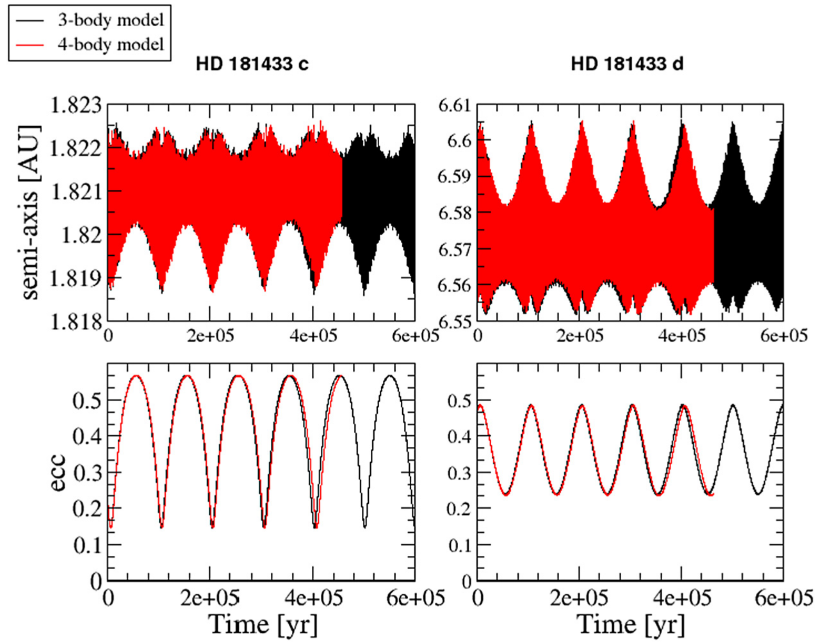

Fig. 5. Evolution of the semi-major axis and eccentricity of the two major planets considering the 4 and 3 body problem.

3.4. ICs in a line segment of a_2

Firstly, we took a set of ICs on a segment of the outer planet semi-major axis, being 4AU $\leq a_2 \leq$ 6.5AU, and fixed all the other orbital parameters to their nominal values given in Table 1). Though the interval excludes the nominal position of the system (a_{20} = 6.6 AU), there is no loss of meaning in regard to our illustrative purpose.

Using the Ncorp code [28] developed by our group, we integrated a set of 600 ICs inside the defined range of the outer planet semi-major axis for a total integration time $T = 10^9$ years and a sampling step $h = 10^2$ years, in order to monitoring the instability time-scales of the system in the considered region of the phase space. Fig. 6 presents the results of such integrations, where the vertical axis shows the corresponding escape times[2] of each IC in the considered interval with the upper limit 10^9 years.

Notice the prominent structures indicating a fast increase in the predicted lifetime of the system which coincide with the nominal positions of high-order MMRs, namely the 4/1, 5/1 and 6/1 MMR, highlighted with red lines in Fig. 6. Such resonances seem to provide a protective mechanism for those initial conditions lying inside them from the quick instabilities arising in their surroundings. With a lighter red tone, we have also indicated in the figure the nominal position of the weaker 9/2 and 11/2 MMRs. Furthermore, a considerable dispersion between adjacent points can be observed, e.g. the region separating the nominal resonances (4.5 AU $< a_2 <$ 5.5 AU) or ICs with $a_2 \gtrsim$ 5.5 AU. Recall that there are lifetime values separated by less than 0.1 AU that differ up to almost two orders of magnitude. Even considering the intrinsic numerical errors due to the integration, such a dispersion points out the intrinsic chaoticity associated to the dynamics of the system around this region.

For the same set of ICs both, S and D_S were computed. Our routine operates a rescaling of the system time–space dimensions such that the initial outer semi-major axis is taken as $a_2^* = 1$ AU (the "$*$" symbol indicates a rescaled quantity): let $\eta > 0$ be a factor that either can expand or compress the system's real architecture, i.e $a_i^* = \eta a_i$ and such that the code admits that $\eta =$ 1AU$/a_2$. It is easy to verify that the intrinsic time-scales of the system (orbital periods and therefore, the secular and resonant periods) are also rescaled by a factor that goes as $\sim \eta^{3/2}$.

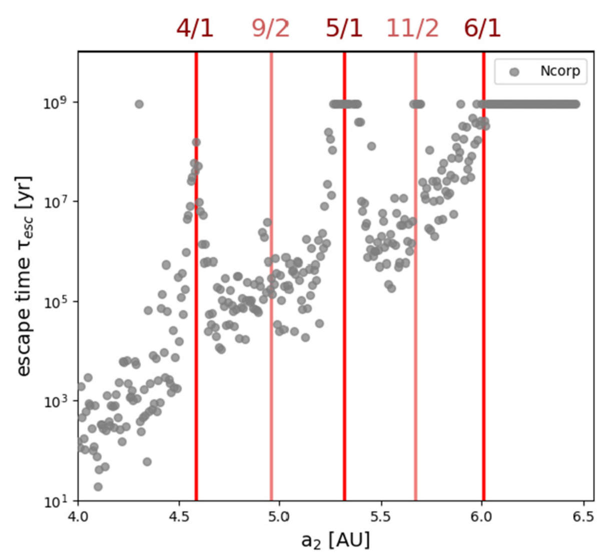

Fig. 6. Distribution of 600 ICs integrated in the range [4.0, 6.5] AU of the outer semi-major axis a_2, with their corresponding system lifetime. The straight lines indicate the nominal position of some resonances present in the region. Our numerical solutions show with reasonable resolution the changes in the instability time-scales of the system as one approaches the resonances' locations.

We introduce a partition box based on the concepts of a macroscopic orbital stability (in the Hill's criteria) [41]. For each planet, the partition box can be thought as a rectangular area in the system's phase space, with extensions $[-\Delta a_i, \Delta a_i] \times [-\Delta e_i, \Delta e_i]$, and where the center is occupied by the specific pair (a_i, e_i) of the IC that is being evaluated. The subindex $i =$

[2] In the present work, we call "escape time" the instant at which the system is destroyed as a consequence of the dynamical features of the trajectories: either both orbits approach each other to distances with high probability of collision, or the system is driven into planetary scattering processes, causing the ejection of the outer body or the inner one to "fall onto" the central star.

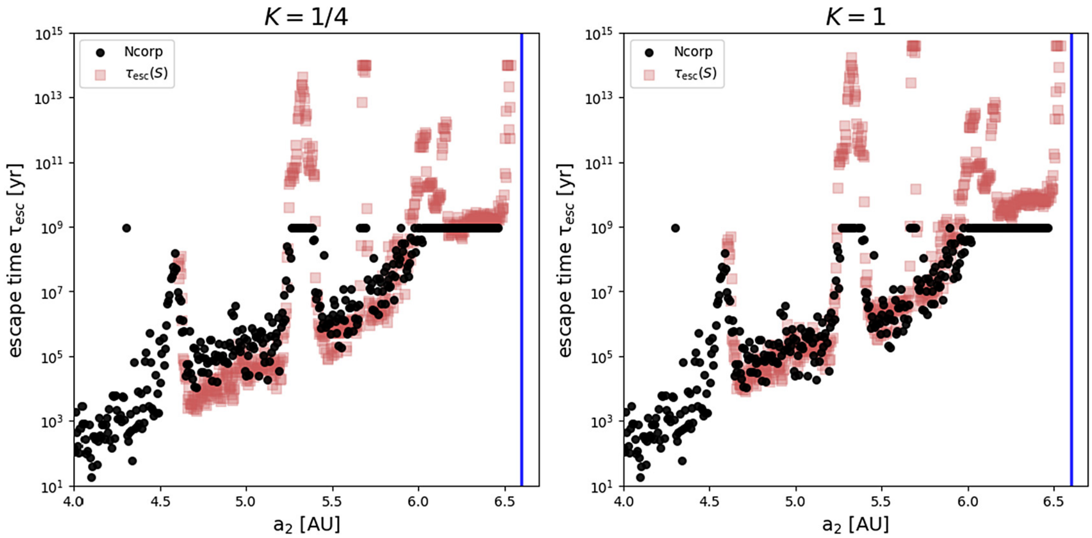

Fig. 7. Comparison between the "pure" numerical integrations (Fig. 6) and estimations of instability timescales using the Shannon approach. We show the results considering two values for the proportionality factor K. The blue line highlights the nominal position of the semi-major axis a_{20} corresponding to the outer planet.

1, 2 corresponds to the inner and outer planets respectively. Notice that a global diffusion coefficient D_S is estimated for the trajectories described by each orbiting body. We took $\Delta a_1 = \Delta a_2 = \Delta_h$, where

$$\Delta_h = 2\sqrt{3}R_H; \qquad R_H = \left[\frac{(m_1 + m_2)}{3m_0}\right]^{1/3} \frac{(a_1 + a_2)}{2}, \tag{19}$$

R_H being the mutual Hill's radius of the planets and where m_0 is the star mass. In regard to the eccentricities, we set $\Delta e_1 = \Delta e_2 = 0.5$ (the singular cases $e_i - \Delta e_i < 0$ or $e_i + \Delta e_i > 1$ are "naturally" avoided through internal conditions of the routine). Afterwards, we used these values of Δa_i and Δe_i to reconstruct the box in terms of Delaunay-like variables L_i and G_i, such that besides the respective mass factors and gravitational constant, $L_i = a_i$ and $G_i = a_i(1 - e_i^2)$, $i = 1, 2$. Thus defined, L, G are the square of the classical Delaunay variables (factors aside). In fact it proved to be more adequate to deal with a diffusion coefficient in terms of variables sharing the same dimensions.

We used a partition of $q = 1600 \times 1600$ cells and the total integration time T was defined as the minimum value between forty times the (rescaled) secular period of the system, T_{sec}, and 10^5 yrs. The sampling rate h is such that the total number of orbital points, $N = T/h$, be ten times the value of q and hence $N/q_0 = 10q/q_0 \gg 1$.

In this particular application the time derivative of the entropy was computed by means of a least square fit over the full evolution of $S(t)$. Indeed, the entropy requires the values of the variables $(L_i(t), G_i(t))$ and to get a confident value of dS/dt, it should be $T \gg T_{sec}$, i.e. the system should run for a sufficient long time in order to avoid periodicities introduced by the secular terms. If the motion time is less than the secular period, then the values of S, D_S are not accurate and this fact restricts the computations to $a_2 > 4.5$ UA (see Fig. 6).

Finally, each IC was integrated together with an ensemble of ten other "ghost-systems" surrounding the central IC with infinitesimally close displacements ($\sim 10^{-3}$ around both variables a_i and e_i).

Fig. 7 shows a comparison between the escape time estimated via the Shannon approach $\tau_{esc}(S)$ (red squares) and the values outcoming from the crude numerical integration of the equations of motion (as the ones in Fig. 6) (black dots). The value of $\tau_{esc}(S)$ corresponding to a given IC was obtained as follows: For each planet, a coefficient $D_{S,i}$ and an escape time $\tau_{esc,i}$ are derived in the fashion

$$D_{S,i} = \frac{\sigma(L_i, G_i)}{q} q_{0,i}(t)\dot{S}_i(t); \qquad \tau_{esc,i} = K\frac{(\Delta L_i)^2 + (\Delta G_i)^2}{D_{S,i}}, \tag{20}$$

where $\sigma(L_i, G_i) = (L_{\max,i} - L_{\min,i})(G_{\max,i} - G_{\min,i})$ is the maximum area reached out by the phase variables (L_i, G_i) of each trajectory during the elapsed time, while the numerator in the expression of $\tau_{esc,i}$ is given by a quarter of the extent of the partition box in the action-variables (L_i, G_i) centered in the IC. Then the final estimate for the global escape time of the system was acquired as the minimum of the individual escape times, $\tau_{esc} = \min\{\tau_{esc,1}, \tau_{esc,2}\}$.

We tested two different values for the K factor, whose magnitude may be attached to the dynamics of the system, more precisely to the direction in which diffusion proceeds. In Fig. 7, we observe that $K = 1$ shows a very reasonable agreement with the results coming from the long term integrations of the Ncorp code. Notwithstanding, it is noticeable the sharply structures outlined by the red squares in both panels, coincident with the nominal positions of the MMRs highlighted in Fig. 6.

3.5. Dynamical maps: MEGNO vs escape-time

In this section we focus on the comparison of dynamical maps for the system HD 181433 obtained by two different approaches, one using a classical chaos indicator, the MEGNO, and another one by means of τ_{esc}.

Fig. 8 displays such dynamical maps constructed in a given (a_2, e_2) domain of the HD 181433 system's phase space. The left-hand panel shows a map parameterized by the MEGNO indicator, $\langle Y \rangle$, computed over a 10^5 yrs time-span and considering a grid of 100×100 initial values of (a_2, e_2), with 4.5 AU $\leq a_2 \leq$ 10AU and $e_2 \in [0.0, 0.8]$. The computation of the MEGNO was performed by the Ncorp routine [28], applying the same Bulirsh–Stoer integrator but with precision $ll = 13$ and a sampling rate of $h = 1$ year. Those ICs leading to collisions or escapes before 10^5 yrs are depicted in white.

The right-hand panel of Fig. 8 presents a dynamical map for the diffusion estimates in the same region of the phase plane, (a_2, e_2), i.e. a τ_{esc}-map. We adopted the same grid of 100×100 ICs as in the MEGNO map that were integrated also for a 10^5 yrs time-span and h such that the total number of orbital points $N = 5q$ for $n_e = 5$ "ghost-systems". We took the same partition as

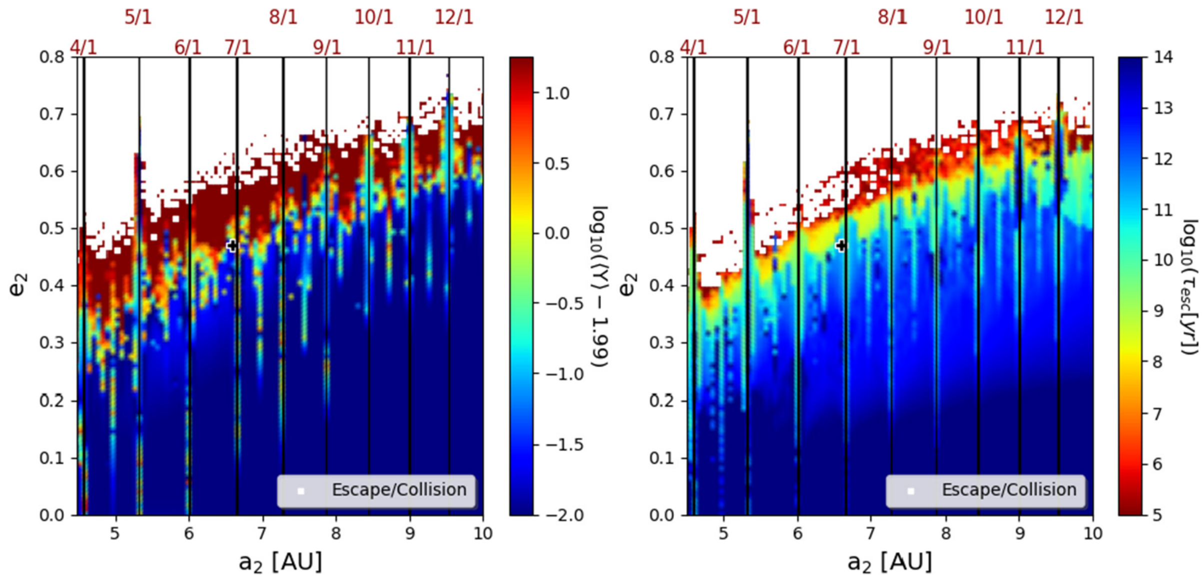

Fig. 8. A MEGNO map (left) and a $\tau_{\rm esc}$-map (right) in the (a_2, e_2) plane corresponding to the same ICs for HD 181433. The black cross indicates the nominal position of the system, while the black lines highlight other MMRs present in the phase space. ICs leading to collisions or escapes before 10^5 yrs are depicted in white.

before, $q = 1600 \times 1600$ cells onto the boxes in the (a_i, e_i)-planes, with $\Delta a_i = \Delta_h$ and $\Delta e_i = 0.5$ $(i = 1, 2)$ and afterwards both the boxes and the cells were redefined in terms of Delaunay-like variables to perform the computations.

From the estimate of the diffusion coefficients $D_{S,i}$, $i = 1, 2$ for each ensemble, we derived the corresponding escape time, $\tau_{\rm esc}$, that provides a measure of the instability time-scales of the HD 181433 system. Notice the qualitative agreement between both maps. Indeed, in general, the Shannon estimates of the system's lifetime shows a correspondence with the indications of regularity/irregularity provided by the MEGNO-map. Also, the $\tau_{\rm esc}$-map shows that regions of almost stability (large lifetimes) are coincident with the presence of several MMRs, besides the 4/1, 5/1 and 6/1 already discussed, for values of $a_2 > 7$AU the 7/1, 8/1, 9/1, 10/1 and 12/1 commensurabilities also appear. The nominal position of the system lies in a region with escape time $\tau_{\rm esc} \sim 10^{10}$ years, very close to unstable solutions of high eccentricities $(e_2 > 0.5)$ and more stable solutions for $e_2 < 0.4$, corroborating then the results given in [39].

Furthermore, we should highlight the quantitative information revealed by the $\tau_{\rm esc}$-map against a more qualitative picture provided by the MEGNO-map. Notice the gradient of the system life-time observed in the right-hand panel in the transient region between unstable ICs and long-term stable solutions ($10^7 \lesssim \tau_{\rm esc} \lesssim 10^9$) in comparison with the MEGNO-map where such a region is revealed just as chaotic with values $\langle Y \rangle \gg 2$. Recall that the MEGNO-map was performed considering a single IC while the $\tau_{\rm esc}$-map involves ensembles around the given IC, thus some quite unstable solutions accordingly to their MEGNO values appear as collisions/escapes in the $\tau_{\rm esc}$-map, as expected.

4. Conclusions

The Shannon entropy proves to be a very efficient tool to display the global and local dynamics of a high-dimensional system as well as to provide accurate estimates of the diffusion rate. Its computation is rather simple, it just requires a counting box scheme after solving the equations of motion of the system for a given ensemble of initial conditions and the computation of the mean time derivative of the entropy evolution.

Herein an improvement of the best choice of the partition is given, the size of the unit cell depends on the character of the diffusion, i.e. rather confined or extended in action space, that leads to a larger or smaller surface density of iterates on the adopted section.

The application to a 4D map reveals its efficiency to estimate time-scales for chaotic instabilities in relatively short motion times in comparison with the ones derived from the diffusion coefficient obtained from the variance evolution. Indeed, dealing with $n_p = 1000$ nearby initial conditions iterated up to 5×10^6, i.e, 5×10^9 iterates, the exponent b is far from the expected value for nearly normal diffusion ($b \approx 1$) and thus, the obtained numerical value of the diffusion coefficient is quite inaccurate. As discussed, maybe for larger motion times it would approximate its actual value. On the other hand, for similar values of n_p and total number of iterates, the Shannon entropy approach provides a value of the escape time quite close to the actual one obtained from direct numerical simulations (see [27] for more details about the required computational effort in simple models).

Particularly interesting is the implementation of this technique to a real physical problem as the 3BP. As a main difference with respect to any dynamical indicator based on the evolution of the tangent vector, the computation of D_S or $\tau_{\rm esc}$ does not require the solution of the first variational equations. Moreover, the escape time for each planet in the system can be derived, while in general this cannot be done when the variational equations are involved in the computation.

The computational effort to derive $\tau_{\rm esc}$, for a given time-span, is nearly the same as the one required to compute the MEGNO when considering 10 "ghost-systems" in the entropy code for the HD 181433 system. While the actual escape-time should be obtained from N-body simulations over a time-span of the order of the life-time of the host star, the one derived by means of the present approach requires much shorter integrations but provides information about the stability of the system over large times-scale as Fig. 7 reveals.

The MEGNO as well as all chaos indicators is useful to separate regular and chaotic components of phase space but they do not furnish any information about the speed of chaotic diffusion. In this direction the escape-time map provides, besides the same dynamical information as a MEGNO-map (for instance the MMR resonance structure), the actual time-scale of stability of the system as shown in Fig. 8.

Therefore a combination of different techniques would furnish a very efficient way to investigate the global dynamics in any high-dimensional system. A general picture of the structure of the phase space would be revealed by any fast indicator, which should supply information on the location of invariant manifolds, resonances, quasiperiodic and chaotic regions. Since chaos indicators could not distinguish between stable and unstable chaos, the entropy approach should be included in order to get a measure of the time-rate of the instabilities arising in those chaotic domains of physical interest.

CRediT authorship contribution statement

Pablo M. Cincotta: Conceptualization, Methodology, Software, Formal analysis, Writing - original draft, Writing - review & editing. **Claudia M. Giordano:** Conceptualization, Methodology, Software, Formal analysis, Writing - original draft, Writing - review & editing. **Raphael Alves Silva:** Conceptualization, Methodology, Software, Formal analysis, Writing - original draft, Writing - review & editing. **Cristián Beaugé:** Conceptualization, Methodology, Software, Formal analysis, Writing - original draft, Writing - review & editing.

Declaration of competing interest

The authors declare that they have no known competing financial interests or personal relationships that could have appeared to influence the work reported in this paper.

Acknowledgments

This work was supported by grants from Consejo Nacional de Investigaciones Científicas y Técnicas de la República Argentina (CONICET), the Universidad Nacional de La Plata and the Universidad Nacional de Córdoba, IAG-Universidade de São Paulo and CAPES. We are most thankful to the referees for their valuable suggestions and comments that have allowed us to improve the manuscript.

References

[1] G. Benettin, L. Galgani, A. Giorgilli, J.M. Strelcyn, Meccanica 15 Part I: Theory, 9-20; Part II: Numerical Applications, 1980, pp. 21–30.

[2] P.M. Cincotta, C.M. Giordano, C. Simó, Phase space structure of multi-dimensional systems by means of the mean exponential growth factor of nearby orbits, Physica D 182 (2003) 11.

[3] P.M. Cincotta, C.M. Giordano, Theory and applications of the mean exponential growth factor of nearby orbits (MEGNO) method, Lecture Notes in Phys. 915 (2016) 93.

[4] J. Laskar, The chaotic motion of the solar system. A numerical estimate of the size of the chaotic zones, Icarus 88 (1990) 266.

[5] J. Laskar, Frequency analysis for multi-dimensional systems. Global dynamics and diffusion, Physica D 67 (1993) 257.

[6] A.J. Lichtenberg, M.A. Lieberman, Regular and Stochastic Motion, Springer Verlag, New York, 1994.

[7] C. Froeschlé, E. Lega, On the structure of symplectic mappings. The fast Lyapunov indicator: A very sensitive tool, Celestial Mech. Dynam. Astronom. 78 (2000) 167.

[8] M. Guzzo, E. Lega, C. Froeschlé, On the numerical detection of the effective stability of chaotic motions in quasi-integrable systems, Physica D 163 (2002) 1.

[9] E. Lega, M. Guzzo, C. Froeschlé, Theory and applications of the fast Lyapunov indicator (FLI) method, Lecture Notes in Phys. 915 (2016) 35.

[10] P.M. Cincotta, C. Simó, Simple tools to study global dynamics in non-axisymmetric galactic potentials -I, Astron. Astrophys. Suppl. Ser. 147 (2000) 205.

[11] Ch. Skokos, On the stability of periodic orbits of high dimensional autonomous Hamiltonian systems, Physica D 159 (2001) 155.

[12] Ch. Skokos, T.C. Bountis, Ch. Antonopoulos, Geometrical properties of local dynamics in Hamiltonian systems: The generalized alignment index (GALI) method, Physica D 231 (2007) 30.

[13] Ch. Skokos, T. Manos, The smaller (SALI) and the generalized (GALI) alignment indices: Efficient methods of chaos detection, Lecture Notes in Phys. 915 (2016) 129.

[14] M. Fouchard, E. Lega, C. Froeschlé, C. Froeschlé, On the relationship between fast Lyapunov indicator and periodic orbits for continuous flows, Celestial Mech. Dynam. Astronom. 83 (2002) v205.

[15] R. Barrio, Sensitivity tools vs. Poincaré sections, Chaos Solitons Fractals 25 (2005) 711.

[16] R. Barrio, Theory and applications of the orthogonal fast Lyapunov indicator (OFLI and OFLI2) methods, Lecture Notes in Phys. 915 (2016) 55.

[17] A. Milani, A.M. Nobili, An example of stable chaos in the solar system, Nature 357 (1992) 569.

[18] L.H. Miranda Filho, M.A. Amato, Y. Elskens, T. Rocha Filho, Contribution of individual degrees of freedom to Lyapunov vectors in many-body systems, Commun. Nonlinear Sci. Numer. Simul. 74 (2019) 236.

[19] B. Many Manda, B. Senyange, Ch. Skokos, Chaotic wave-packet spreading in two-dimensional disordered nonlinear lattices, Phys. Rev. E 101 032206.

[20] P.M. Cincotta, C.M. Giordano, J.G. Martí, C. Beaugé, On the chaotic diffusion in multidimensional Hamiltonian systems, Celestial Mech. Dynam. Astronom. 130 (2018) article id. #7, 23 pp.

[21] B.V. Chirikov, A universal instability of many-dimensional oscillator systems, Phys. Rep. 52 (1979) 263.

[22] N. Miguel, C. Simó, A. Vieiro, On the effect of islands in the diffusive properties of the standard map, for large parameter values, Found. Comput. Math. 15 (2014) 89.

[23] T. Manos, M. Robnik, Survey on the role of accelerator modes for anomalous diffusion: The case of the standard map, Phys. Rev. E 89 (2014) 022905.

[24] M. Harsoula, G. Contopoulos, Global and local diffusion in the standard map, Phys. Rev. E 97 (2018) 022215.

[25] P.M. Cincotta, I.I. Shevchenko, Correlations in area preserving maps: A Shannon entropy approach, Physica D (2019) 132235, http://dx.doi.org/10.1016/j.physd.2019.132235.

[26] P.M. Cincotta, C. Simó, Global dynamics and diffusion in the rational standard map, Physica D 413 (2020) 132661.

[27] C.M. Giordano, P.M. Cincotta, The Shannon entropy as a measure of diffusion in multidimensional dynamical systems, Celestial Mech. Dynam. Astronom. 130 (2018) article id. N°35.

[28] C. Beaugé, P.M. Cincotta, Shannon entropy applied to the planar restricted three-body problem, Celestial Mech. Dynam. Astronom. 131 (2019) 52.

[29] V.I. Arnold, On the nonstability of dynamical systems with many degrees of freedom, Sov. Math. Dokl. 5 (1964) 581–585.

[30] P.M. Cincotta, C.M. Giordano, Phase correlations in chaotic dynamics: A Shannon entropy measure, Celestial Mech. Dynam. Astronom. 130 (2018) 74.

[31] P.M. Cincotta, C.M. Giordano, R. Alves Silva, C. Beaugé, Shannon entropy diffusion estimates: Sensitivity on the parameters of the method, Celestial Mech. Dynam. Astronom. (2020) in press (available at http://fcaglp.fcaglp.unlp.edu.ar/~pmc/PAPERS-SUB/CELE-D-20-00032.pdf).

[32] C. Shannon, W. Weaver, The Mathematical Theory of Communication, Urbana, Illinois U.P., 1949.

[33] A. Lesne, Shannon entropy: A rigorous notion at the crossroads between probability, information theory, dynamical systems and statistical physics, Math. Struct. Comput. Sci. 24 (2014) e240311.

[34] V. Arnol'd, A. Avez, Ergodic Problems of Classical Mechanics, second ed., Addison-Wesley, New York, 1989.

[35] V. Gelfreich, C. Simó, A. Vieiro, A dynamics of 4*D* symplectic maps near a double resonance, Physica D 243 (2013) 92.

[36] E. Lega, C. Froeschlé, M. Guzzo, Diffusion in Hamiltonian quasi-integrable systems, Lecture Notes in Phys. 729 (2008) 29.

[37] F. Bouchy, M. Mayor, C. Lovis, et al., The harps search for southern extra-solar planets. XVII. Super-Earth and Neptune-mass planets in multiple planet systems HD 47186 and HD 181433, Astron. Astrophys. 496 (1814) 527.

[38] G. Campanella, Treating dynamical stability as an observable: A 5:2 mean motion resonance configuration for the extrasolar system HD 181433, Mon. Not. R. Astron. Soc. 418 (1814) 1028.

[39] G. Horner, R. Wittenmyer, D. Wright, et al., 33 planetary system: Dynamics and a new orbital solution, Astron. Astrophys. 158 (1814).

[40] K. Batygin, K.M. Deck, M.J. Holman, Dynamical evolution of multi-resonant systems: The case of GJ 876, Astron. J. 149 (2015) 167.

[41] C. Marchal, G. Bozis, Hill stability and distance curves for the general three-body problem, Celestial Mech. Dynam. Astronom. 26 (1982) 311.